Integrating melt electrospinning writing and microfluidics to engineer a human cardiac microenvironment for high-fidelity drug screening

Yu-hong Wang [a,b,c,1], Ting-ting Liu [d,1], Yan-ping Guo [c,e,1], Shuo-ji Zhu [b,c,f,1],
Zi-ming Liao [a], Jia-mei Song [a], Xi-ming Zhu [a], Jia-liang Liang [b,c], Moussa Ide Nasser [b,c],
Nan-bo Liu [b,c,**], De-hua Chang [g,***], Ping Zhu [b,c,****], Bin Yao [a,*]

[a] Academy of Medical Engineering and Translational Medicine, Tianjin University, 300072, China
[b] Guangdong Cardiovascular Institute, Guangdong Provincial People's Hospital (Guangdong Academy of Medical Sciences), Southern Medical University, Guangzhou, Guangdong, 510100, China
[c] Guangdong Provincial Key Laboratory of Pathogenesis, Targeted Prevention and Treatment of Heart Disease, Guangzhou Key Laboratory of Cardiac Pathogenesis and Prevention, Guangdong, 510100, China
[d] Department of Laboratory Diagnosis, The 971th Hospital, Qingdao, China
[e] School of Medicine, South China University of Technology, 510641, China
[f] Department of Cardiac Surgery, The University of Tokyo Hospital, Tokyo, 113-8654, Japan
[g] Department of Cell Therapy in Regenerative Medicine, University of Tokyo Hospital, Tokyo, 113-8654, Japan

ARTICLE INFO

ABSTRACT

The preclinical evaluation of drug-induced cardiotoxicity is critical for developing novel drug, helping to avoid drug wastage and post-marketing withdrawal. Although human induced pluripotent stem cell-derived cardiomyocytes (iPSC-CMs) and the engineered heart organoid have been used for drug screening and mimicking disease models, they are always limited by the immaturity and lack of functionality of the cardiomyocytes. In this study, we constructed a Cardiomyocytes-on-a-Chip (CoC) that combines micro-grooves (MGs) and circulating mechanical stimulation to recapitulate the well-organized structure and stable beating of myocardial tissue. The phenotypic changes and maturation of CMs cultured on the CoC have been verified and can be used for the evaluation of cardiotoxicity and cardioprotective drug responses. Taken together, these results highlight the ability of our myocardial microarray platform to accurately reflect clinical behaviour, underscoring its potential as a powerful pre-clinical tool for assessing drug response and toxicity.

1. Introduction

Cardiovascular disease (CVD), including myocardial infarction (MI), is a major global economic burden and a leading cause of patient mortality. Drug therapy is one of the primary means of treating myocardial infarction and reducing mortality [1]. Preclinical research on drug-induced cardiotoxicity is critical to drug development, as it is a significant factor contributing to drug withdrawal. Drug-induced cardiotoxicity, a detrimental adverse event, perturbs the cardiovascular system's physiological equilibrium. It has emerged as a pivotal concern within the realms of drug development and public health [2,3]. Currently, the leading platforms for drug screening are conventional cell cultures and animal models. Nonetheless, conventional cell cultures exist in a two-dimensional environment devoid of cell-cell interactions and cell-extracellular matrix interactions. There are also distinctions in interspecies relations between animals and humans. Consequently,

Scheme. 1. Characteristics and Applications of CoC.

these platforms exhibit considerable disparities in effectiveness and adverse effects relative to human studies, limiting their further implementation [4]. In conclusion, there is an urgent need to develop new platforms for the detection of drug-induced cardiotoxicity (see Scheme 1).

iPSC-CMs exhibit many characteristics of cardiac cells, including the ability to contract and respond to electrical signals, making them a promising tool for drug screening [5,6]. However, iPSC-derived cardiomyocytes are significantly immature compared to adult cardiomyocytes, exhibiting a phenotype similar to that of fetal cells [7]. The lack of maturity of iPSC-CMs compared to their adult counterparts may alter their response to drug candidates. To bridge this gap, scientists have proposed numerous methods to promote the maturation of iPSC-CMs, primarily by mimicking the physiological environment of the heart. Mechanical stimulation, which plays a crucial role in cardiac development, can effectively promote the maturation of iPSC-CMs by applying mechanical stretch that simulates the preload of normal myocardium [8,9]. Other methods include prolonging culture time [10, 11], co-culture with different cell types [12], culturing iPSC-CMs on parallel microstructures [13–15], using substrates with myocardial stiffness [16], conductive extracellular matrices [17], electrical stimulation [13,18] and small chemical molecules [19]. It seems that the combination of two or more methods to treat iPSC-CMs can achieve better results [20–22].Therefore, it is necessary to integrate several

techniques and develop new platforms to improve the maturation of iPSC-CMs and achieve a phenotype closer to that of native adult cardiomyocytes. This will help to obtain data that more closely resembles that of the adult.

At the same time, the alignment of cardiomyocytes contributes to the anisotropic tissue structure of the heart, which is critical for effective electrical activation and synchronized contractile activity of the tissue [23]. In many myocardial diseases, deformation and remodelling of the myocardial interstitial network occurs, affecting myocardial contractile function and perfusion [24]. Furthermore, cell alignment has been shown to be one of the most important parameters affecting the function of engineered cardiac tissue [21,25–29]. Motlagh [30] has posited that surface topography have an impact on cardiomyocyte shape, gene expression and protein distribution. Wong [31], on the other hand, suggests that such surface topographies promote cellular alignment and potentiate the pro-maturational effects of other factors, such as hormonal stimulation and electrical cues. According to previous studies, MGs are one of the most common methods to guide the directional alignment of cells [25,32]. With the development of microfabrication technology, Melt Electrospinning Writing (MEW) is an emerging technique that combines melt electrospinning with 3D printing, enabling the precise positioning of sub-micron fibres to create structures with higher precision and reproducibility than conventional 3D printing technologies. Furthermore, by using the patterns constructed by MEW as
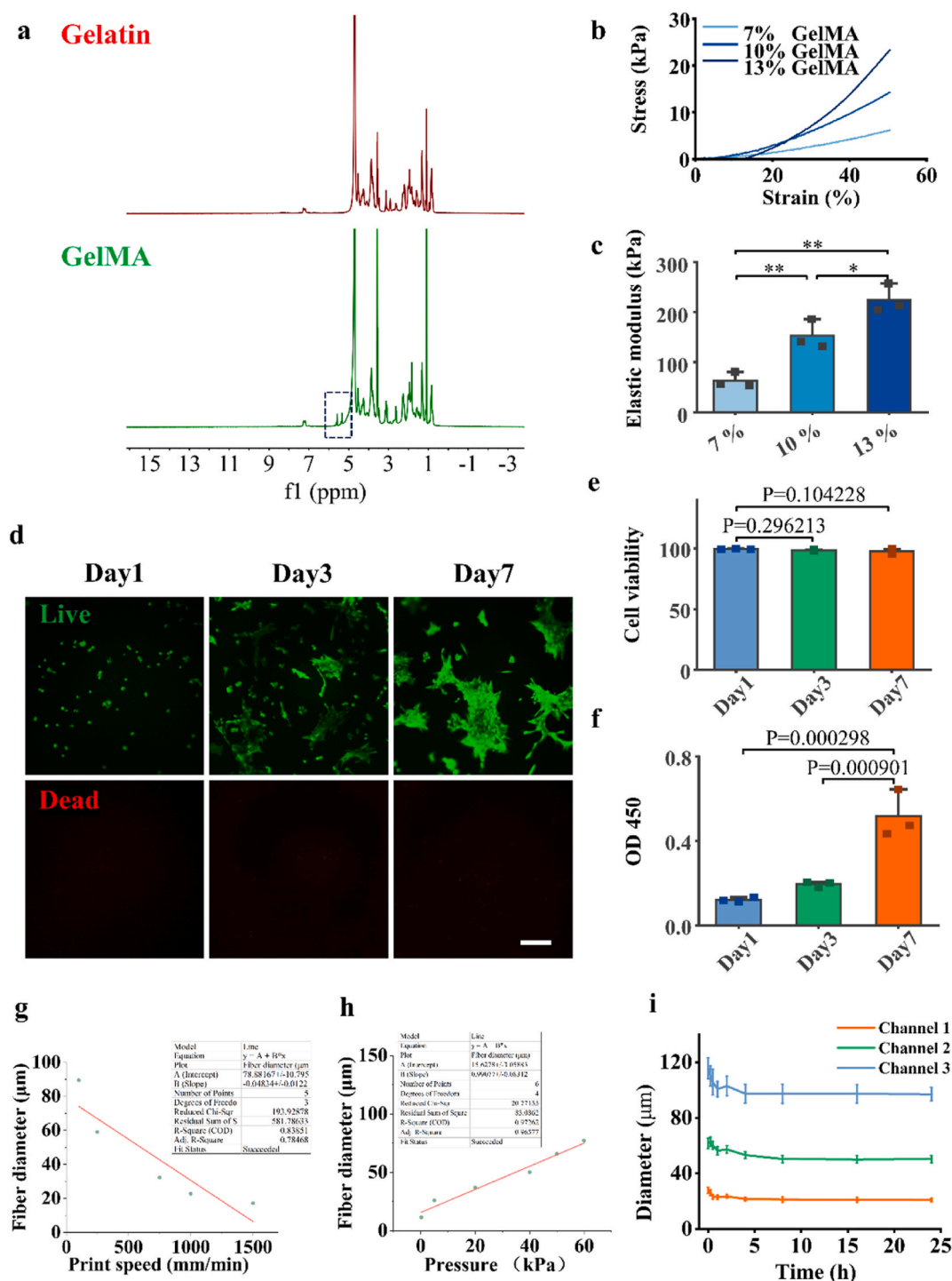
Fig. 1. (a) NMR spectroscopy of gelatin and GelMA. (b) Stress-strain curves for different concentrations of GelMA. (c) The elastic modulus for different concentrations of GelMA. (d) Live/dead staining of AC16 cells co-cultured with GelMA for days 1, 3 and 7. Scale bars = 100 µm. (e) Quantitative cell viability maps based on live/dead imaging. (f) cck8 assay for cell viability. (g–h) Fiber diameter as a function of print speed and extrusion pressure. (i) Effect of swelling on channel diameter.

sacrificial materials, a variety of topological structures can be built on biocompatible hydrogels to induce directed cell growth [32].

In this study, we aimed to design and develop a CoC platform characterized by: 1) ease of fabrication, 2) controllable maturation of iPSC-CMs, and 3) scalability for screening a variety of drug candidates. We selected Gelatin Methacryloyl (GelMA), which has an elastic modulus similar to that of heart tissue, as the extracellular matrix for cell culture, and constructed a hydrogel with MGs using MEW technology combined with casting. At the same time, integration into a microfluidic system provides cyclic mechanical stimulation to promote the maturation of iPSC-CMs. As an in vitro model, we further verified the platform's response to the positive inotropic drug isoproterenol (ISO). Furthermore, to demonstrate the versatility of the platform to study cardiotoxicity and cardioprotective effects, we selected the clinically approved drug doxorubicin (DOX) as a candidate drug to study drug-induced cardiotoxicity and ivabradine (IVA) as a candidate drug to mitigate cardiac toxicity (Fig. 1).

2. Materials and methods

2.1. Materials

AC16 cell line (NO. CTCC-003-0014) and Human induced pluripotent stem cells (hiPSCs) (NO. 30HU-002-400212) was purchased from Meisen Chinese Tissue Culture Collections (Zhejiang, China). ISO (NO. HY-B0468), DOX (NO. HY-15142), IVA (NO. HY-B0162AS), CHIR99021 (NO. HY-10182), Wnt-C59 (NO. HY-15659), Cyclophosphamide (CP) (NO. HY-17420) and Thiazovivin (NO. HY-13257) were purchased from MCE (USA). Accutase™ (NO. 07922) and mTeSR™1 (NO. 85850) were purchased from complete medium (Stem Cell Technologies, USA). Live/dead assays kit (NO. C2015S), 4 % paraformaldehyde solution (NO. P0099-100 ml), 0.3 % Triton X-100 (NO. P0096-100 ml), 3 % bovine serum albumin (BSA) (NO. P0268-100 ml), Actin-Tracker Green-488 (NO. C2201S), Cell Counting Kit-8 (NO. C0037), LDH Cytotoxicity Assay Kit (NO. C0016) and Reactive Oxygen Species Assay Kit (NO. S0033S) were purchased from Beyotime (Beijing, China). Anti-alpha Actinin (NO. ab90421), Anti-Cardiac Troponin T (NO. ab209813), Anti-Connexin 43 (NO. ab312836), goat anti-rabbit Alexa Fluor 488 (NO. ab150077) and goat anti-mouse Alexa Fluor 555 (NO. ab150118) were purchased from Abcam (USA). DAPI (NO. D1306) was purchased from Thermo Fisher Scientific (USA). Gelatin (NO. 9000-70-8) was purchased from Sigma (USA). Dulbecco's Modified Eagle Medium/Nutrient Mixture F-12 (DMEM/F12) (NO. 11320033) and RPMI 1640 medium (NO. 11875093) were purchased from Gibco (USA).

2.2. Synthesis of GelMA

GelMA was synthesized by reacting gelatin with methacrylic anhydride as previously reported [33,34]. The process commenced with the dissolution of 10 g of gelatin in 100 mL of PBS at a temperature of 50 °C. Subsequently, 5 mL of methacrylic anhydride was introduced dropwise to the gelatin solution, and the mixture was stirred continuously at the same temperature for 2 h to facilitate the reaction. The reaction was subsequently quenched by diluting the mixture with 100 mL of pre-warmed PBS for 10 min, ensuring the termination of the polymerization process. To eliminate any residual salts and unreacted methacrylic anhydride, the resultant solution underwent dialysis against distilled water for a period of one week at a controlled temperature of 45 °C, utilizing dialysis tubes with a molecular weight cut-off of 12–14 kDa. The purified GelMA solution, characterized by its fibrous, white, and foam-like appearance, was then subjected to lyophilization for five days using a vacuum freeze dryer (Jinteng Experimental Equipment Co., Ltd, China) to yield a solid product. The obtained GelMA was stored at a temperature of −20 °C for subsequent utilization in experiments.

2.3. GelMA characterization

Characterization of Gelatin and GelMA was performed using proton nuclear magnetic resonance spectroscopy (1H NMR). The 1H NMR analysis was executed on a 500 MHz spectrometer with the samples dissolved in deuterium oxide. The spectral data were subsequently processed utilizing MestReNova software to elucidate the chemical structure and confirm the successful modification of gelatin to GelMA.

2.4. Mechanical properties

The preparation of GelMA involved casting the formulated inks into rectangular molds with dimensions of 9 × 9 × 2 mm. 0.5 % (w/v) irgacure 2959 was used to photocrosslink the ink to make it suitable for subsequent compression testing. To ensure accuracy in the analysis, the exact dimensions of each sample were ascertained using a digital caliper prior to testing.

To mitigate the effects of hydrogel swelling, the photocrosslinked hydrogels were immersed in PBS for a period of 24 h prior to compression testing to achieve swelling equilibrium. The photocrosslinked hydrogels were carefully positioned on the platform of a universal testing machine (INSTRON, 3345). The tests were performed with the maximum displacement set at half the initial thickness of the specimens at a controlled compression rate of 0.05 mm/s. This method enabled the calculation of the compressive modulus for each sample, ascertained by determining the gradient of the linear segment of the stress-strain (S-S) curve, confined to the initial 20 % strain. Each experimental group was subjected to this standardized testing procedure, with a minimum of three replicates ($n = 3$) to ensure the reliability and reproducibility of the data obtained.

2.5. Biocompatibility of GelMA

The AC16 cell line was employed for the assessment of the biomaterial's biocompatibility. Live/dead assays were conducted on days one, three, and seven of the culture period. Calcein AM and propidium iodide (PI) were separately diluted to final concentrations of 2 μM and 8 μM, respectively, using Dulbecco's phosphate-buffered saline (DPBS). This is in accordance with the instructions provided by the manufacturer (Beyotime, China). DPBS washings were performed three times at each given timepoint. Subsequently, the Calcein AM/PI mixture was introduced. Following a 30-min incubation period at 37 °C in the absence of light, the constructs were washed three times. Subsequently, imaging was conducted using a microscope (Nikon, Japan). Green and red fluorescence represented viable and non-viable cells, respectively. For each sample, three random images were captured and analyzed using ImageJ software. The percentage of cell viability was calculated by dividing the number of live cells by the total number of cells counted [35].

Prepare the CCK8 working solution according to the manufacturer's instructions, which involves diluting the CCK8 concentrate 10-fold with DMEM/F12 medium. On days 1, 3, and 7 of cell culture, first rinse the cells once with PBS, then add the CCK8 working solution and incubate at 37 °C in the dark for 30 min. Subsequently, measure the absorbance at 450 nm using a microplate reader. Set up a blank group containing CCK8 working solution without cells to account for background absorption, and subtract the values of the blank group from each experimental group to minimize error.

2.6. Constructing MGs by MEW

Hydrogels with MGs were synthesized using a method adapted from Ref. [32]. MEW 3D printing technology (BP6601, EFL-Tech Co.,Ltd, Suzhou, China) was employed to deposit polycaprolactone (PCL) onto a substrate with high precision, following predesigned printing paths. Subsequently, the PCL fibers were encapsulated within a frame (inner diameter = 10*8*3 mm) and 200ul of hydrogel precursor solution was poured into the frame. Photo-crosslinking was employed to induce the polymerization and solidification of the hydrogel precursor. Once the hydrogel had fully cured, the PCL fibers, which were now embedded within the hydrogel matrix, were carefully detached from the substrate. At this point, a 10*8*2.5 mm hydrogel with MGs was obtained.

2.7. The effects of swelling on MGs

Following the separation of PLC fibers from the hydrogel, initial microchannels were established. The dimensions of these microchannels were approximately equivalent to the pre-determined fiber diameters. Subsequently, the hydrogels were incubated at 37 °C in an oven with the addition of phosphate-buffered saline (PBS). Microscopic measurements of the microchannel diameters were taken at pre-specified time intervals: 0 min, 15 min, 30 min, 1 h, 2 h, 4 h, 8 h, 16 h, and 24 h following immersion in PBS. The hydrogel precursor employed in this study was a 10 % (w/v) GelMA solution.

2.8. Construction of chips and microfluidic platforms

The upper and lower layers of the PDMS (polydimethylsiloxane) chip were fabricated by pouring a PDMS precursor, with a base-to-curing agent weight ratio of 11:1, onto a mold created from laser-cut polymethyl methacrylate (PMMA) and curing it at 60 °C for 3 h. The precursor was selected based on its ability to facilitate the fabrication of the desired structure while maintaining the necessary mechanical properties. The thickness of the lower layer is 4 mm, and its interior contains a rectangular cavity ($24 \times 10 \times 3$ mm) and two approximate triangular side chambers (largest side $= 8 \times 6 \times 3$ mm). The rectangular cavity was designed to accommodate a hydrogel and cell culture medium, while the lateral chambers on either side were intended for the attachment of microfluidic channels. The upper layer is 1 mm thick and contains a window with dimensions of $10 \times 8 \times 1$ mm (when bonded to the lower layer, the window is directly above the hydrogel and between the two side chambers), which is used to manipulate the lower rectangular cavity. The above layers were subsequently bonded together by plasma treatment. The aforementioned layers were subsequently bonded together via plasma treatment. Prior to use, the final structures were sterilized by UV light and rinsed several times with ethanol (70 % v/v) and DPBS. Forty-eight hours after the addition of cells, hydrogels with MGs were adhered to the cell culture cavity of PDMS.

The microfluidic platform was constructed in accordance with the methodology proposed by Huang [36], with modifications made to the parameters.

2.9. iPSCs culture and CMs differentiation

iPSCs were seeded into dishes coated with Matrigel (Corning, USA), and diluted to a ratio of 1:100 with DMEM/F12. The cells were cultured in mTeSR™1 complete medium at a temperature of 37 °C within an incubator maintained at 5 % CO2. Upon reaching 85 % confluence, the iPSCs were passaged using Accutase™ and subsequently cultured in mTeSR™1 complete medium that had been supplemented with 2 μM Thiazovivin for 12 h. Following this treatment, the cells were maintained in mTeSR™1 complete medium.

Cardiomyocyte (CM) differentiation was induced using a protocol adapted from previous studies [37]. Cells were initially cultured and expanded until they reached approximately 90 % confluence. At this point, the growth medium was replaced with Cardiac Differentiation Medium 3 (CDM3), which was composed of RPMI 1640 medium, supplemented with 500 μg/ml of recombinant human serum albumin derived from Oryza sativa (Aladdin, China, NO. 20901ES03), and 213 μg/ml of L-ascorbic acid 2-phosphate trisodium salt (TargetMol, USA, NO. T2185). The medium was refreshed every 48 h. For day 0 to day 2, the culture medium was further supplemented with 5 μM of the GSK-3 inhibitor CHIR99021 to promote mesodermal differentiation. On day 2, the medium was switched to CDM3, which was additionally supplemented with 2 μM of the Wnt pathway inhibitor Wnt-C59 to enhance cardiac specification. Following this, on day 4, the medium was reverted to CDM3 alone and was subsequently changed every 48 h. The onset of cell contraction was first observed around day 7. On day 10, iPSC-CMs were digested by 0.25 % trypsin-edta for 5 min and resuspended at a density of 5×10^5. 500ul of cell suspension was added to the MGs side of each hydrogel and cells were observed to resume beating the next day.

Subsequently, the hydrogel laden with cells was meticulously positioned within the rectangular cavity of the PDMS chip. At this point, the long axis of the hydrogel is perpendicular to the long axis of the rectangular cavity of the chip, precisely located between the two side chambers. A minute quantity of α-cyanoacrylate-based medical adhesive was applied to facilitate the bonding between the hydrogel and the chip.

2.10. Immunofluorescence

An immunofluorescence analysis was conducted on cells cultured in confocal dishes. Cell fixation was performed with 4 % paraformaldehyde for 15 min. After fixation, the samples were perfused with 0.3 % Triton X-100 for 15 min. After permeabilization, the cells were incubated with 3 % bovine serum albumin for 2 h at room temperature to reduce non-specific antibody binding. Subsequently, the cells were incubated with primary antibodies (Anti-alpha Actinin (diluted 1:100), Anti-Cardiac Troponin T (diluted 1:300), Anti-Connexin 43 (diluted 1:500)), respectively, overnight at 4 °C to allow for antibody-antigen interaction. On the following day, the cells were incubated with the appropriate secondary antibodies (goat anti-rabbit Alexa Fluor 488 (diluted 1:500), goat anti-mouse Alexa Fluor 555 (diluted 1:500)) for 2 h at room temperature in the dark to ensure fluorescence signal development.

For nucleus visualization, cells were counterstained with DAPI solution for 10 min at 37 °C. Additionally, the cytoskeleton was counterstained using Actin-Tracker Green-488 to highlight filamentous actin structures. Following the staining procedures, images were acquired using a laser scanning confocal microscope (Leica, Germany) and subsequently analyzed with ImageJ software.

2.11. Calcium imaging and beating recording

Fluo-4 AM calcium indicator was used for calcium imaging. Briefly, samples were rinsed three times with DPBS to remove any residual media. Subsequently, the samples were incubated with a loading buffer consisting of 1 ml of Krebs-Hensleit's Solution (Pricella, China, NO. PB180348) containing 4 μM Fluo-4 AM (Beyotime, China, NO. S1060), $1 \times$ PowerLoad™ concentrate (Thermo Fisher Scientific, USA, P10020), and 2.5 mM Probenecid (Thermo Fisher Scientific, USA, NO. P10020). This incubation was performed at 37 °C for 1 h in the dark to protect the fluorescent indicators from light-induced degradation. After the incubation period, the samples were rinsed three times with DPBS to remove excess dye and unbound indicators. Finally, the samples were visualized for fluorescence signals using a fluorescence microscope (Nikon, Japan). ImageJ was then used to analyze the calcium transient videos.

The contractile function of the cardiomyocytes was assessed by recording their beating. Brightfield videos of the cardiomyocyte cultures were captured using a microscope (Nikon, Japan). These videos were then analyzed using ImageJ software to determine the beating frequency of the cells, which indicates the cells' contractile activity [38].

2.12. ROS test

The assessment of reactive oxygen species (ROS) was conducted according to the instructions provided with the Reactive Oxygen Species Assay Kit. Briefly, the samples were rinsed three times with DPBS to remove any residual media. Subsequently, the samples were incubated with DMEM/F12 containing 10 μM 2′,7′-dichlorodihydrofluorescein diacetate (DCFH-DA) at room temperature in the dark for 20 min. This incubation allows for the cellular uptake and deacetylation of DCFH-DA, leading to the formation of the fluorescent compound 2′,7′-dichlorofluorescein (DCF) upon oxidation by ROS. Following the incubation period, the samples were rinsed three additional times with DPBS to remove excess DCFH-DA and unconverted reagent. The fluorescence signals indicative of ROS production were then captured using a fluorescence microscope (Nikon, Japan). A minimum of three image sets per sample were collected to ensure representative data acquisition. Finally, the images were analyzed using ImageJ software to quantify the fluorescence intensity, which correlates with the levels of ROS in the samples.

2.13. Statistic analysis

SPSS 26 and Origin 2022 were used for statistical analysis and graphing of the data. For the comparison of multiple groups where the data were normally distributed, one-way ANOVA was conducted, followed by HSD post hoc test. When the analysis involved two groups with
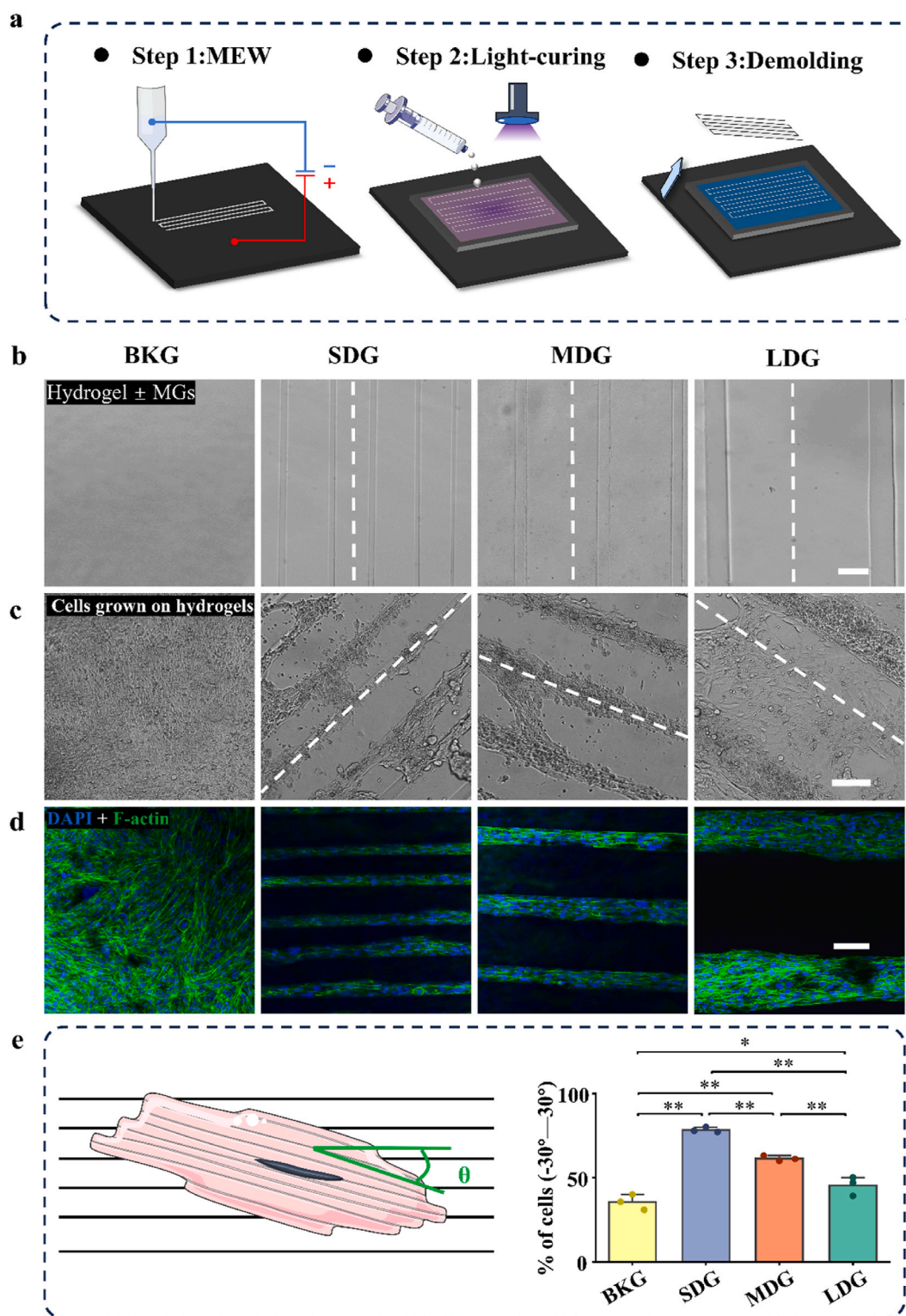
Fig. 2. (a) Steps for the construction of hydrogels with MGs. (b) Bright-field image of the hydrogel with MG after demolding (dashed lines represent the orientation of MGs). Scale bars = 100 μm. (c) Bright-field images of AC16 cells grown on hydrogels with MGs (dashed lines represent the orientation of the MGs). Scale bars = 100 μm. (d) Confocal fluorescence images of AC16 cells grown on hydrogels with MGs. Scale bars = 100 μm. (e) The ratio of the angle between the nucleus and the MGs is between −30° and 30°. (* and ** show statistical significance at p < 0.05 and p < 0.01, respectively).

normally distributed data, an independent two-sample *t*-test was applied. If not otherwise specified, the methods used are those described above. For datasets that did not conform to a normal distribution, nonparametric statistical analysis was performed using the Kruskal-Wallis H test to assess differences among groups. Post hoc pairwise comparisons were conducted with Bonferroni correction applied to mitigate the risk of type I errors associated with multiple testing. Statistical significance was determined at the p < 0.05 level. Each experimental condition was replicated at least three times. Data are presented as mean ± standard deviation (SD).

3. Results and discussion

3.1. Hydrogel characterizations

GelMA, a highly versatile biomaterial, is derived from the chemical modification of gelatin via the introduction of methacrylate groups onto the reactive amine and hydroxyl functional groups present on the side chains of its constituent amino acids, utilizing methacrylic anhydride as the crosslinking agent. This synthetic procedure confers upon GelMA enhanced mechanical properties and biocompatibility, positioning it as a prominent material in various biomedical applications, including cell culture, bio-3D printing, and tissue engineering [39].NMR spectroscopic analysis of both gelatin and its derivative GelMA was conducted to characterize the chemical modifications. The spectra exhibited distinct features, with the appearance of new peaks at 5.45 and 5.69 ppm, which correspond to the vinyl protons of the methacrylate groups. These spectral alterations serve as definitive evidence for the successful methacrylation of gelatin, as illustrated in Fig. 1a. The distinct peaks indicate the presence of the methacrylate groups within the GelMA structure, confirming the covalent attachment post-synthetic modification.

The mechanical properties of hydrogels are of paramount importance as they directly influence cell fate. An ideal biomaterial should exhibit mechanical properties that are analogous to those of native cardiac tissue [40]. It has been documented that the Young's modulus of native cardiac tissue oscillates between 200 and 500 kPa during contraction and 10 and 20 kPa during relaxation [41]. To identify the optimal hydrogel concentration with suitable mechanical properties, GelMA was prepared at concentrations of 7 %, 10 %, and 13 %. The results of the compression analysis indicated that the elastic moduli were 63.49 ± 14.86, 152.74 ± 28.82, and 224.61 ± 28.22 kPa (n = 3) (Fig. 1b and c). Subsequently, the 10 % GelMA was selected for further experimentation, as it falls within Young's modulus range of native myocardium and exhibits resilience under cyclic mechanical stretching.

To ascertain the suitability of our synthesized GelMA for sustained cell cultivation, we conducted a co-culture with AC16 cells using a 10 % GelMA substrate. Live-dead assays were performed at the junctures of day 1, day 3, and day 7 post-seeding to assess the viability of the cells. The findings indicated that the ratio exceeded 90 % across all time points assessed (Fig. 1d–f). These results show that there is no decrease in cell viability in cultures up to 7 days, indicating the good biocompatibility of 10 % GelMA.

3.2. Construction of hydrogels with MGs

The fabrication of a hydrogel with MGs was achieved through a three-step process. At the outset of the process, we utilized MEW to print the requisite patterns. Subsequently, the hydrogel was created through the processes of casting and photopolymerization. The final step involved the removal of the mold, thereby yielding the hydrogels with MGs. In this context, polycaprolactone (PCL) served as the bioink, which was used to construct micro-patterns. The fiber mold formed by this material is relatively soft, allowing for gentle detachment from the hydrogel, thereby achieving non-destructive demolding. Moreover, this material can be melted into a liquid state at 65 °C and generate micrometer-scale fibers under the influence of extrusion force and electrostatic forces. It has been demonstrated that this method is capable of producing channels with diameters ranging from 500 nm to 100 μm, along with high-precision patterned microstructures [32]. Separate experiments were conducted with varying print speeds and extrusion pressures to ascertain the relationship between different printing parameters and the resulting fiber diameter. The results of these experiments are presented in Fig. 1g and h.

To construct microchannels on the hydrogel with controllable dimensions and patterns, a series of experiments was conducted to investigate the impact of hydrogel swelling on channel size (Fig. 1i).

Three channel sizes were created: large, medium, and small, with initial dimensions of 115.66 ± 7.40, 61.5 ± 3.77, and 27.99 ± 2.25, respectively. The hydrogels were immersed in PBS and maintained at 37 °C to simulate the conditions typically encountered in cell culture. Irregular swelling of the hydrogels was observed at the onset of immersion, characterized by an increase in hydrogel volume and a reduction in the diameter of the surface microchannels. This swelling process was observed to cease after approximately seven to 9 h. At this point, the stabilized diameters of the large, medium, and small channels were measured to be 97.03 ± 4.89, 50.30 ± 2.66, and 20.79 ± 1.26, respectively. When the immersion time was extended to 24 h, it was found that the channel diameters obtained were essentially the same as those observed at 9 h. In summary, swelling resulted in a change in channel size, the extent of which depended on the initial diameter. The stabilization period of the channels was approximately 9 h.

3.3. MGs promote oriented alignment of AC16 cells

In order to provide a microenvironment that is analogous to the extracellular matrix and serves as physical cues to guide cell alignment, we constructed micrometer-scale patterns with parallel structures by controlling the printing path within a computer (Fig. 2a). To investigate the impact of the topological structure diameter on cellular behavior, two groups were established: the Blank group (BKG) and the microgrooved structures group (MGsG). The BKG served as a control group, while the MGsG included three subgroups: the Small diameter group (SDG), the Medium diameter group (MDG), and the Large diameter group (LDG). After solvation equilibrium, the channel diameters of SDG, MDG, and LDG were approximately 0, 20 μm, 50 μm, and 100 μm, respectively (Fig. 2b and Fig. S1). The specific printing parameters are presented in Fig. S2.

The AC16 cells display a fibroblast-like morphology and demonstrate the capacity for indefinite proliferation. Furthermore, they demonstrate excellent adhesion to the culture surface, growing well without the need for Matrigel or gelatin pre-treatment of the culture dishes, which facilitates our study of the interactions between cells and microstructures. Following a three-day incubation period, microscopic observation revealed that the majority of cells within the MGsG exhibited growth along the channels (dashed lines indicate the direction of the MGs) (Fig. 2c). Following a seven-day period, an examination of the expression of DAPI and f-actin was conducted under a confocal microscope. The MGs enhanced the alignment of AC16 cel, with a greater degree of nucleus orientation observed as the diameter of the MGs decreased. In contrast, cells in the BKG showed an irregular arrangement, with nuclei pointing in random directions (Fig. 2d). A further analysis was conducted to determine the proportion of cells with an angle between the cell nuclei and the MGs ranging from $-30°$ to $30°$. The results demonstrated frequencies of 35.42 % for the BKG, 78.30 % for the SDG, 61.38 % for the MDG, and 45.33 % for the LDG (Fig. 2e).

3.4. MGs promote oriented alignment of iPSC-CMs

By the tenth day of iPSC differentiation, we confirmed the successful specification of cardiomyocytes by detecting the expression of signature proteins that are characteristic of these cells (Fig. S3). Unlike AC16 cells, iPSC-CMs, when digested into single cells, aggregate and self-assemble into tightly packed cell clusters. This is because the synchronized contraction of cardiac tissue relies on the rapid transmission of electrical signals through mature and closely connected CMs. Anatomically, cardiomyocytes are primarily composed of an interwoven and branched network structure interconnected through gap junctions, which is essential for the heart's effective blood pumping during systolic and diastolic movements [42]. After 7 days of culture, we observed that iPSC-CMs formed a network-like structure (Fig. S4, with dashed lines indicating the direction of the MGs). To assess the arrangement of cells at the MGs, we performed immunofluorescence analysis with DAPI and
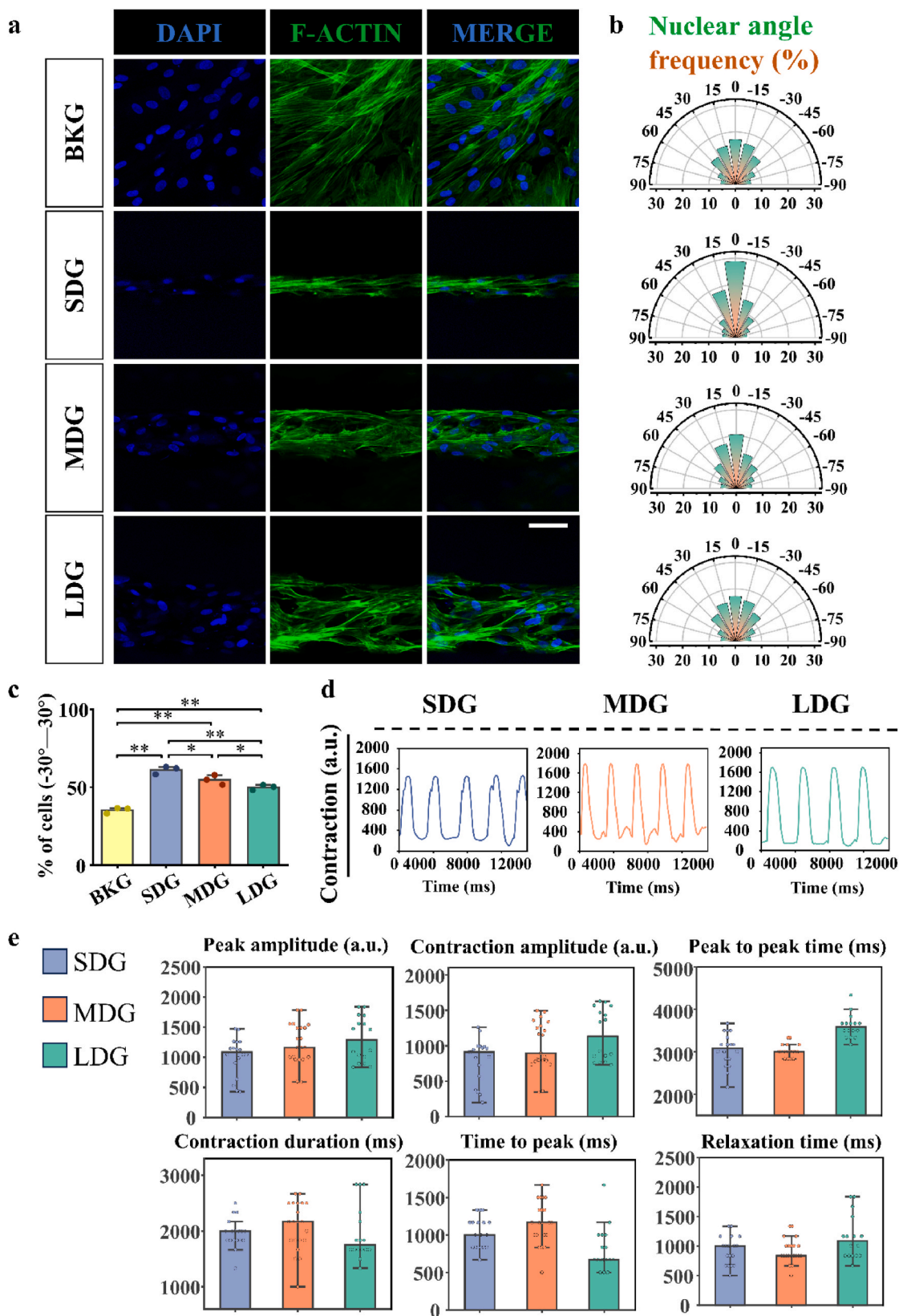
Fig. 3. (a) Confocal fluorescence images of the nucleus and cytoskeleton of iPSC-CMs. Scale bars = 10 μm. (b) Orientation distribution of the long axis of the nucleus. (c) The ratio of the angle between the nucleus and the MGs is between −30° and 30°. (* and ** show statistical significance at $p < 0.05$ and $p < 0.01$, respectively). (d) Beating curves of iPSC-CMs in the MGsG. (e) Statistical analysis based on CMs beating curves. (Nonparametric statistical analyses were performed using the Kruskal-Wallis H test and post hoc pairwise comparisons using the Bonferroni correction, with the median representing the centralized trend of the data.)
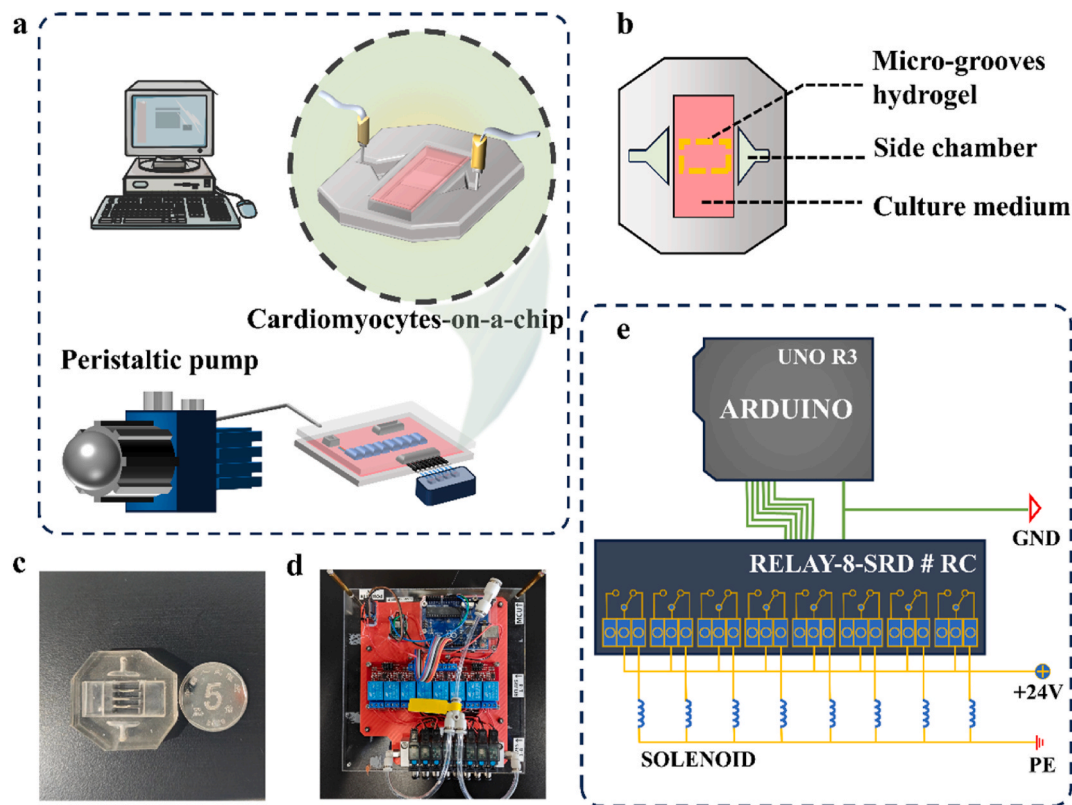
Fig. 4. (a) Main components of the CoC platform. (b) Schematic structure of PDMS chip.(c) Physical drawing of PDMS chip. (d) Physical drawing of the microfluidic platform. (e) Structural diagram of the microfluidic platform.

f-actin to quantify the proportion of cells with the angle between the cell nuclei and the MGs within −30°–30°. The results indicated frequencies of 35.29 % for the BKG, 61.10 % for the SDG, 54.74 % for the MDG, and 49.93 % for the LDG (Fig. 3a–c). In summary, for both AC16 cells and iPSC-CMs, the frequency of cell nuclei orientation within −30°–30° was the highest in the SDG.

In addition to the alignment of CMs, the beating behavior is a critical factor in this process. As our hydrogel substrate precludes direct measurement of contractile force, we utilized the MUSCLEMOTION software to quantify cellular contractile activity. This software is commonly utilized in the investigation of tissue-engineered myocardium, and it has been demonstrated to demonstrate a robust linear correlation between the contractile amplitude assessed for engineered heart tissues (EHTs) and the contractile force [38]. A beating analysis was conducted on iPSC-CMs cultured in MGsG for 14 days (Fig. 3d and Fig. S5). The relative contractile amplitude, peak contractile amplitude, and contraction time parameters among the groups were not statistically different (Fig. 3e). This may be due to the short duration of cell culture or the MGs being insufficient to affect the pulsatile function of the CMs. Accordingly, the SDG, which exhibited the highest frequency of nuclei orientation between −30° and 30°, was selected as the representative of the micro-grooved groups for subsequent experiments.

3.5. Construction of CoC

Fig. 4a depicts the principal components of the CoC, including multiple chips containing cells, a microfluidic platform linked to a vacuum pump, and a computer that oversees the operational program of the microfluidic platform. The chip is composed of a polydimethylsiloxane (PDMS) chip and a GelMA with MGs containing cardiomyocytes (indicated by the yellow dashed line in the schematic) (Fig. 4b). The PDMS support structure is designed to provide cyclic mechanical actuation and culture medium to the CMs. The cyclic

mechanical actuation is achieved through the use of two side chambers that are connected to the microfluidic platform. The vacuum pump is capable of applying negative pressure to the side chambers through the microfluidic platform. The results of the calculations demonstrate that when negative pressure is applied, there is a change in the longitudinal length of the hydrogel, from 10 mm to 11 mm, resulting in a longitudinal strain of 10 %. Furthermore, the microfluidic platform can be controlled via computer programming, allowing for the implementation of controllable frequency mechanical actuation. A frequency of 1 Hz is employed here, as this is the normal pulsation frequency of the human heart. In addition, due to the limitations of the machine, we take a working pattern of 12 h on and then 12 h off. The culture medium is introduced to both sides of the hydrogel at a volume of 1 ml. Fig. 4c depicts a physical image of the PDMS chip, which is only slightly larger in size than a 50-cent coin. This makes it a convenient and economical choice in terms of material consumption and chip construction.

Fig. 4d and e illustrate the physical and schematic diagrams of the microfluidic platform that was constructed. The microfluidic platform is based on an established and proven design, with the primary components comprising an Arduino UNO R3, a specific model of the relay (RELAY-8-SRD#RC), several solenoid valves, and an array of connecting tubes. The Arduino UNO R3 is an open-source microcontroller development board. By leveraging the company's software suite, it is possible to write and upload code to the board, thereby enabling it to interface with a variety of external hardware devices. This integration allows for the precise control of downstream hardware operations.

3.6. CoC promotes connexin-43 (CX43) upregulation, contractile activity and maturation of calcium transients in CMs

The experimental program is shown in Fig. 5a. To assess the functional capacity of the CM on the CoC, we used immunofluorescence to study the expression of the cardiac marker CX43. CX43 is a pivotal
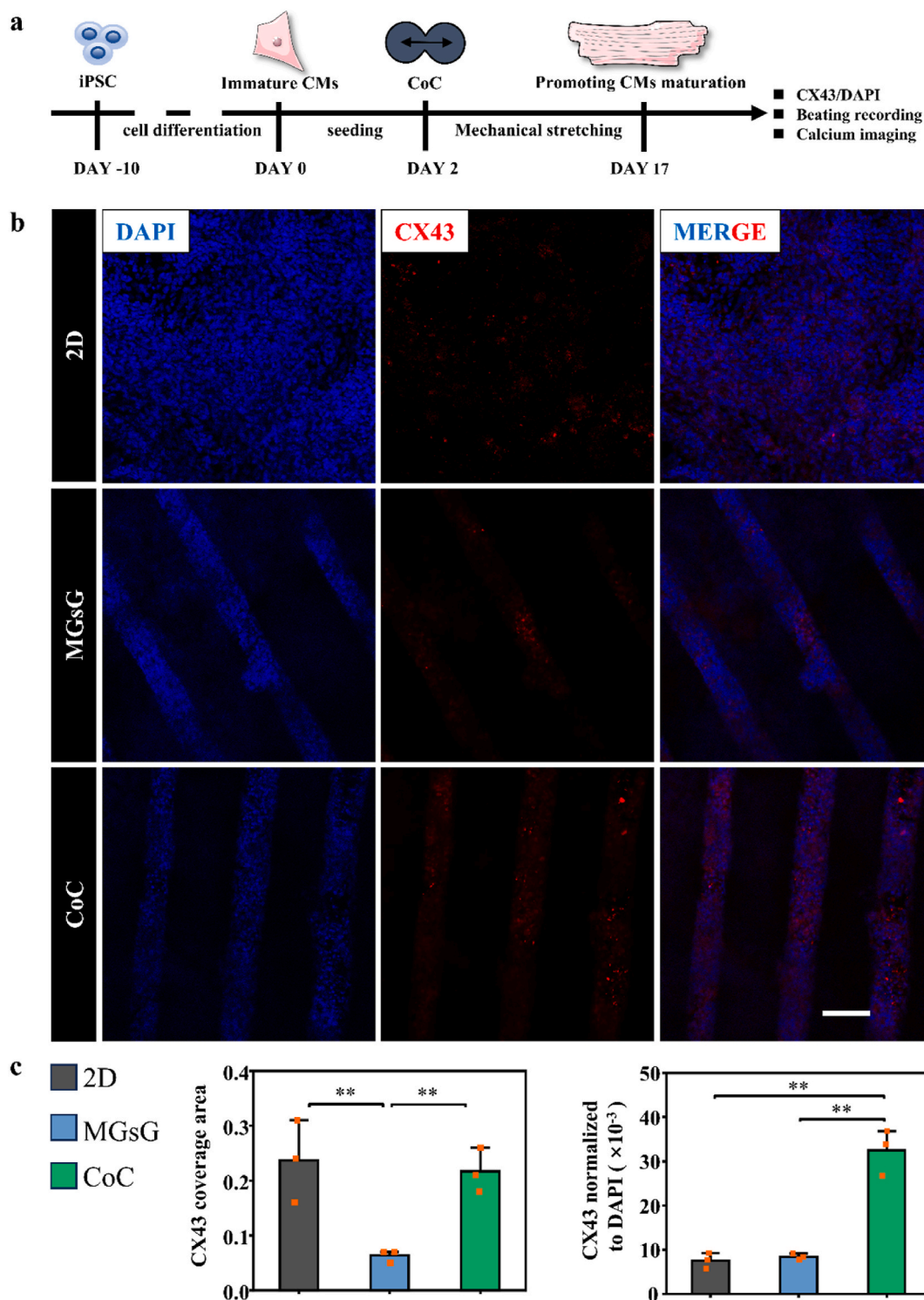
Fig. 5. (a) Schematic timeline of cell differentiation and exposure to mechanical stimuli. (b). Immunofluorescence images of the nucleus and CX43. Scale bars = 100 μm. (c). The fluorescence area of cx43 and the ratio of the fluorescence area of cx43 normalized to DAPI (** shows statistical significance at $p < 0.01$).

protein that facilitates intercellular communication and regulates the electrical coupling between adjacent CMs. After 7 days of culture, we observed that the CoC enhanced the expression of CX43, which is associated with cardiac maturity, indicating that mechanical stimulation promotes the CMs to exhibit improved intercellular connectivity (Fig. 5b and c).

Further, we analyzed the beating activity of each group of CMs. We observed that the CMs on the CoC exhibited deep and slow contractions.

In contrast, cells in the 2D group and MGsG demonstrated shallow and rapid contractions (Fig. 6a and Fig. S6). Specifically, the CoC showed an increase in relative contractile amplitude and peak contractile amplitude compared to other groups, along with prolonged contraction time, time to peak, relaxation time, and the interval between peaks (Fig. 6b). Current research posits that iPSC-CMs resemble fetal cardiomyocytes, exhibiting spontaneous beating behavior. In contrast, adult human ventricular CMs are electrically quiescent without upstream electrical
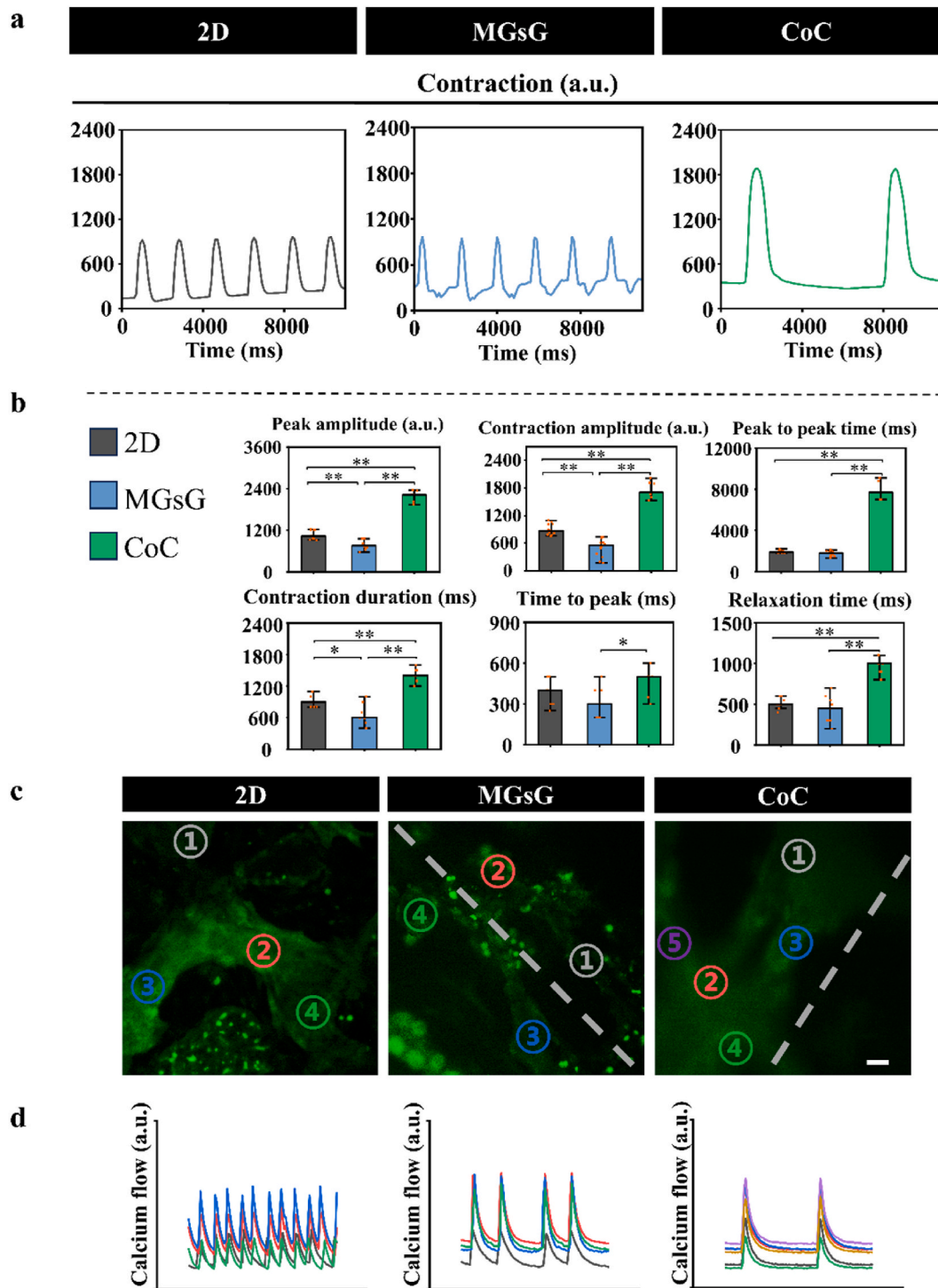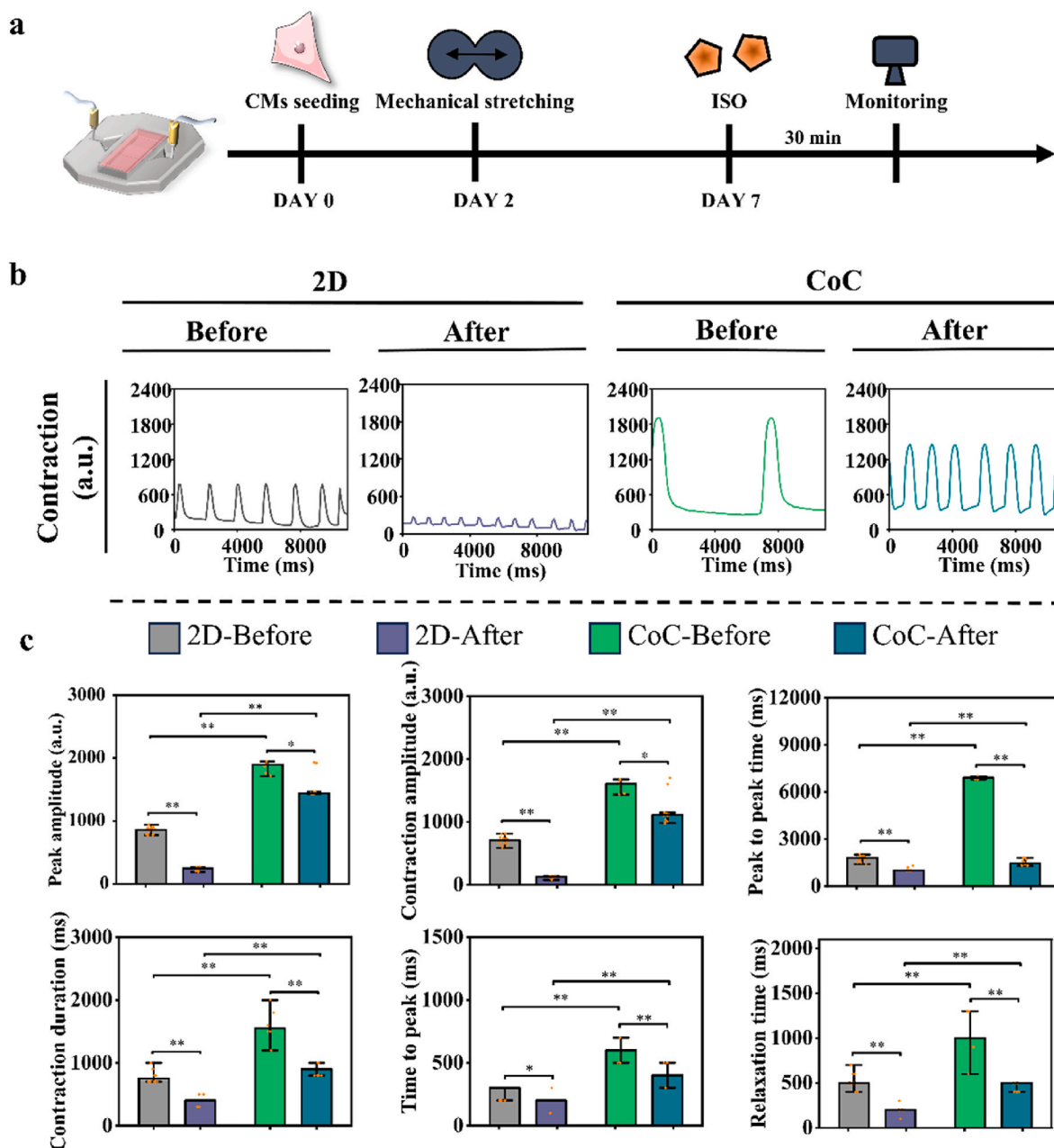
Fig. 6. (a) Beating curves of CMs in 2D, MGsG and CoC. (b) Statistical analysis based on CMs beating curves. (Nonparametric statistical analyses were performed using the Kruskal-Wallis H test and post hoc pairwise comparisons using the Bonferroni correction, with the median representing the centralized trend of the data.) (* and ** show statistical significance at $p < 0.05$ and $p < 0.01$, respectively). (c) Representative fluorescence images and ROIs of CMs loaded with the calcium fluorescent dye Fluo-4 AM. Scale bars = 50 μm. (d) Synchronous calcium transients are acquired from the labeled CMs.

signal stimulation [43]. It is worth noting that the beating frequency of the human fetal heart is typically 120–160 beats per minute, gradually decreasing to 60–100 beats per minute as it matures into an adult heart. This is consistent with the trend of heart rate changes we observed before and after CoC stimulation. This suggests that, compared to the typical 2D cultured hiPSC-CMs, the myocardial cells on the CoC show significant advancement in maturity under the same culture duration.

We also used Fluo-4 for calcium imaging to assess synchronized contraction of cardiac tissue (Fig. 6c). We acquired spontaneous calcium transients in multiple independent regions of interest (ROIs) within the same or adjacent microgrooves (for the 2D group, similar positions were selected) (the dashed lines indicate the direction of the microgrooves). Each group exhibited calcium transient trajectories similar to their respective contractile activities (Fig. 6d). In the MGsG and CoC, better-synchronized pulsations were observed across the ROIs. In contrast, some ROIs in the 2D group showed irregular pulsations. We believe that

Fig. 7. (a) Schematic timeline of ISO evaluations enabled by CoC. (b) Beating curves of CMs in 2D and CoC before and after drug administration. (c) Statistical analysis based on CMs beating curves. (Nonparametric statistical analyses were performed using the Kruskal-Wallis H test and post hoc pairwise comparisons using the Bonferroni correction, with the median representing the centralized trend of the data.) (* and ** show statistical significance at p < 0.05 and p < 0.01, respectively).

these results may indicate that the microgrooves facilitate the synchronized beating of cardiomyocytes.

3.7. CoC has good drug sensitivity for ISO

To demonstrate the feasibility of the CoC as an in vitro drug evaluation platform, we examined its responsiveness to ISO. ISO, which accelerates heart rate and enhances cardiac conduction by activating cardiac β1 receptors, is commonly used to assess drug responses in cardiac tissue [44,45]. Fig. 7a illustrates our experimental protocol, where drug testing was performed on day 7 of culture. Based on the analysis of the beating activity of the cardiomyocytes, we observed that the peak-to-peak time, contraction time, time-to-peak, and relaxation time of the CoC were all reduced after drug treatment (Fig. 7b and

Fig. S7). In particular, the peak-to-peak time showed a significant decrease, with an average change from 6900.00 ± 36.51 (pre-treatment) to 1520.00 ± 61.10 (post-treatment), reflecting a faster heart rate after treatment. Although similar changes were observed in the 2D group, the magnitude of the peak-to-peak time change was smaller, and the contractile amplitude was smaller compared to the CoC group, which may be attributed to its immature characteristics leading to differences in drug response (Fig. 7c). These results indicate that the CoC exhibits superior drug responsiveness compared to traditionally cultured CMs in 2D.

3.8. CoC can be used as an in vitro cardiotoxic drug screen

Accurate preclinical evaluation of drugs can expedite the drug
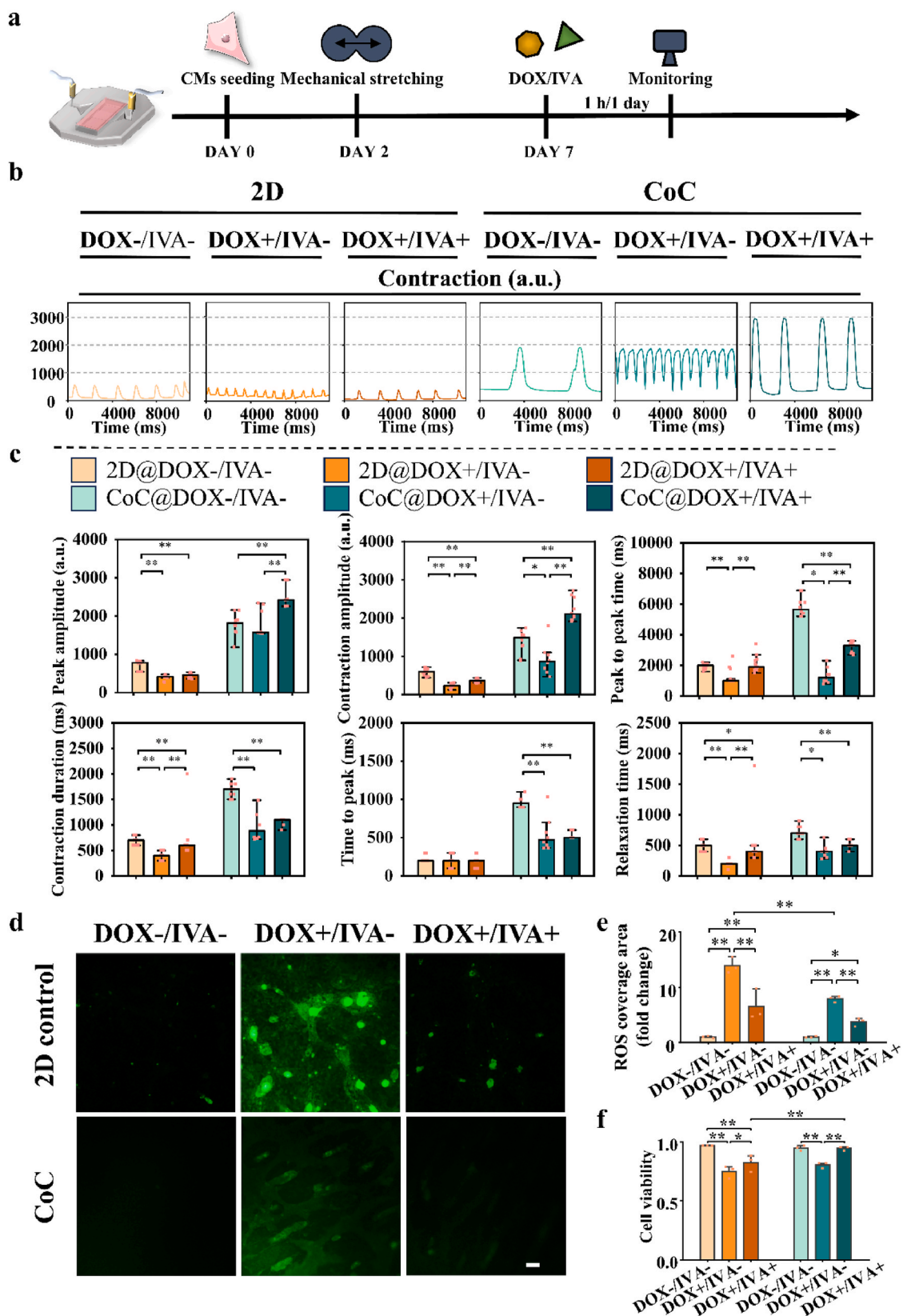
Fig. 8. (a) Schematic timeline of cardiotoxicity and cardioprotective drug evaluations enabled by CoC. (b) Beating curves of CMs in 2D and CoC before and after drug administration. (c) Statistical analysis based on CMs beating curves. (Nonparametric statistical analyses were performed using the Kruskal-Wallis H test and post hoc pairwise comparisons using the Bonferroni correction, with the median representing the centralized trend of the data.). (d) Fluorescence images of ROS in groups of CMs. (e) Quantitative statistical maps based on fluorescence images of reactive oxygen species. Scale bars = 100 μm. (f) Quantitative statistics of CM activity before and after drug administration. (* and ** show statistical significance at p < 0.05 and p < 0.01, respectively).

development process. Therefore, we further evaluated whether the CoC could serve as a candidate screening tool for cardiotoxic or cardioprotective drugs. We selected the clinically used DOX as a model drug to test for cardiotoxicity and IVA as a cardioprotective drug [46]. DOX, a commonly used chemotherapeutic agent, has been shown to have dose-dependent myocardial toxicity. A prevalent cardiac adverse effect associated with DOX is tachycardia, and chronic administration may result in significant myocardial impairment [47]. The mechanism by which this anthracycline drug induces myocardial apoptosis is complex and involves oxidative stress, promotion of apoptotic processes, and ferroptosis [48]. We investigated the cardiotoxicity of DOX at different concentrations (1, and 4 μM). One hour after administration, CMs in the 2D control group exhibited a dose-dependent increase in heart rate in response to DOX (Fig. S8). In addition, we observed gradual apoptosis and necrosis in the CMs 24 h after the addition of DOX (Fig. S9). We chose 1 μM DOX to study its cardiotoxicity on the CoC because cells at this concentration showed reduced viability while still maintaining an assessable beating behavior.

The experimental protocol is depicted in Fig. 8a, where we established DOX-/IVA-, DOX+/IVA+, and DOX+/IVA-groups to investigate the effects of the drugs. In clinical practice, anticancer drugs and cardioprotective drugs are often used in combination to mitigate life-threatening adverse reactions associated with cardiac injury [49]. Therefore, we chose to administer both drugs simultaneously (referring to the DOX+/IVA + group). Moreover, to verify the cardioprotective effect of IVA, we used a concentration of IVA that is twice the dose of DOX (i.e., 2 μM) for the experimental condition. The results of our pre-experiment showed that cardiomyocytes treated with 2 μM IVA had activity comparable to that of untreated cells (Fig. S11). One hour after administration, pulsation analysis results indicated that the DOX+/IVA-group in the CoC exhibited shortened peak-to-peak time, total contraction time, time to peak, and relaxation time, along with varying degrees of decrease in relative contractile amplitude and peak contractile amplitude, indicating that DOX not only caused an increased heart rate but also impaired myocardial contraction (Fig. 8b and Fig. S11). In the group with IVA added (DOX+/IVA+), similar shortening of peak-to-peak time, total contraction time, time-to-peak, and relaxation time was observed. Still, compared to the group without drug addition (DOX-/IVA-group), the addition of IVA resulted in a smaller reduction in peak-to-peak time than that of the DOX+/IVA-group (P < 0.01) (Fig. 8c). More importantly, compared to the DOX+/IVA-group, the contractile amplitude and peak contractile amplitude in the DOX+/IVA + group were preserved or increased. These results demonstrate that IVA inhibited the tachycardia and contractile disorders caused by DOX, which is consistent with the protective effect of IVA in clinical practice by reducing the frequency of myocardium for heart failure patients [46].

Based on the mechanisms by which DOX induces cardiotoxicity, we further assessed the damage caused by ROS using immunofluorescence staining. Twenty-four hours post-administration, we evaluated the relative area coverage percentage of ROS in each group. We found that the CoC produced fewer ROS compared to the 2D group (Fig. 8d and e). This suggests that the CMs on the CoC exhibit a lower degree of damage, which may be attributed to their greater maturity compared to 2D culture conditions. Additionally, the cardioprotective effect of IVA was further confirmed by the results of ROS immunofluorescence staining. Live/dead assays also corroborated the conclusions above conducted 24 h after drug addition (Fig. 8f and Fig. S12). In addition, to demonstrate the universal application of the CoC platform, we also tested the effect of cyclophosphamide (a cardiotoxic drug) (Fig. S13).

Our CoC platform reflects the clinical characteristics of the effects of cardiotoxic and cardioprotective drugs on myocardium, demonstrating different drug responses in terms of beating rate and cell viability compared to traditional in vitro assays. Based on the more mature phenotype of the cardiomyocytes, we believe that the results from the CoC are more closely aligned with clinical efficacy.

4. Conclusions

In summary, we have developed a CoC platform to cultivate mature cardiomyocytes and serve as a candidate drug screening tool. Utilizing MEW technique, we successfully created micro-grooved hydrogels with tunable diameters, facilitating the directed alignment of cells. Our findings indicate that these MGs not only induce cell alignment but also exhibit the capability to synchronize the beating of cardiomyocytes, as evidenced by calcium transient. The integration of this technology into a microfluidic chip system to construct the CoC platform has yielded a system that enhances cardiomyocyte maturation through cyclic mechanical actuation, significantly influencing cell phenotype, beating, and calcium transients.

The CoC platform demonstrated superior drug responsiveness to ISO compared with conventional 2D cultures, underscoring its potential as a more physiologically relevant model. Expanding our investigation to include the assessment of cardiotoxic and cardioprotective drugs, our platform effectively captured the clinical profiles of these medications. This capability highlights the platform's adaptability for evaluating a broad spectrum of drug responses, addressing the escalating need for comprehensive candidate drug testing. The CoC platform, with its ability to mimic the structural and functional attributes of the heart, presents itself as a promising tool for early safety evaluations within the drug development pipeline. Additionally, the efficiency of the entire drug screening process, spanning from cardiomyocyte seeding to the assessment of drug responses within a week, aligns well with the rapid screening requirements of industrial and clinical applications.

Overall, our CoC platform offers a novel avenue for predictive toxicology and pharmacological screening and holds great promise for accelerating the discovery and development of safe and efficacious therapeutics.

CRediT authorship contribution statement

Yu-hong Wang: Writing – review & editing, Writing – original draft, Visualization, Validation, Project administration, Methodology, Investigation, Data curation, Conceptualization. **Ting-ting Liu:** Validation, Supervision, Project administration, Methodology, Investigation. **Yan-ping Guo:** Formal analysis, Data curation, Conceptualization. **Shuo-ji Zhu:** Project administration, Methodology, Investigation. **Zi-ming Liao:** Resources, Project administration, Funding acquisition, Formal analysis, Data curation. **Jia-mei Song:** Validation, Supervision, Software. **Xi-ming Zhu:** Software, Resources, Project administration. **Jia-liang Liang:** Project administration, Methodology. **Moussa Ide Nasser:** Writing – review & editing. **Nan-bo Liu:** Software, Resources, Project administration, Methodology. **De-hua Chang:** Visualization, Validation, Supervision. **Ping Zhu:** Visualization, Validation, Software, Resources, Funding acquisition. **Bin Yao:** Writing – review & editing, Writing – original draft, Investigation, Funding acquisition, Conceptualization.

Ethics approval and consent to participate

This study did not require ethics approval or consent to participate as it did not involve any experimentation on animals. The research was conducted in compliance with all relevant guidelines and regulations.

Declaration of competing interest

De-hua Chang is an editorial board member for Bioactive Materials and was not involved in the editorial review or the decision to publish this article. The authors declare that they have no known competing financial interests or personal relationships that could have appeared to influence the work reported in this paper.

Appendix A. Supplementary data

Supplementary data to this article can be found online at https://doi.org/10.1016/j.bioactmat.2024.11.037.

References

[1] M. Mele, L. Tricarico, R. Ieva, M. Iacoviello, M. Di Biase, N.D. Brunetti, Meta-regression analysis of the impact of medical therapy on long-term mortality in type 2 myocardial infarction, Am. J. Cardiol. 165 (2022) 33–36, https://doi.org/10.1016/j.amjcard.2021.10.044.

[2] M.-Y. Li, L.-M. Peng, X.-P. Chen, Pharmacogenomics in drug-induced cardiotoxicity: current status and the future, Front Cardiovasc Med 9 (2022) 966261, https://doi.org/10.3389/fcvm.2022.966261.

[3] E.W. Esch, A. Bahinski, D. Huh, Organs-on-chips at the frontiers of drug discovery, Nat. Rev. Drug Discov. 14 (2015) 248–260, https://doi.org/10.1038/nrd4539.

[4] Y.-H. Wang, Q. Ouyang, S. Zhao, Y. Zhang, R.-Z. Tian, Y.-P. Guo, R. Zheng, M. I. Nasser, G. Li, P. Zhu, Advances in cardiac organoids, Front. Biosci. 28 (2023) 221, https://doi.org/10.31083/j.fbl2809221.

[5] S. Cho, C. Lee, M.A. Skylar-Scott, S.C. Heilshorn, J.C. Wu, Reconstructing the heart using iPSCs: engineering strategies and applications, J. Mol. Cell. Cardiol. 157 (2021) 56–65, https://doi.org/10.1016/j.yjmcc.2021.04.006.

[6] W. Yang, Q. Ouyang, Z. Zhu, Y. Wu, M. Fan, Y. Liao, X. Guo, Z. Xu, X. Zhang, Y. Zhang, N. Hu, D. Zhang, A biosensing system employing nonlinear dynamic analysis-assisted neural network for drug-induced cardiotoxicity assessment, Biosens. Bioelectron. 222 (2023) 114923, https://doi.org/10.1016/j.bios.2022.114923.

[7] N.T. Feric, M. Radisic, Maturing human pluripotent stem cell-derived cardiomyocytes in human engineered cardiac tissues, Adv. Drug Deliv. Rev. 96 (2016) 110–134, https://doi.org/10.1016/j.addr.2015.04.019.

[8] M.-D. Nguyen, J.P. Tinney, F. Ye, A.A. Elnakib, F. Yuan, A. El-Baz, P. Sethu, B. B. Keller, G.A. Giridharan, Effects of physiologic mechanical stimulation on embryonic chick cardiomyocytes using a microfluidic cardiac cell culture model, Anal. Chem. 87 (2015) 2107–2113, https://doi.org/10.1021/ac503716z.

[9] J.G. Jacot, J.C. Martin, D.L. Hunt, Mechanobiology of cardiomyocyte development, J. Biomech. 43 (2010) 93–98, https://doi.org/10.1016/j.jbiomech.2009.09.014.

[10] Y. Zhou, L. Wang, Z. Liu, S. Alimohamadi, C. Yin, J. Liu, L. Qian, Comparative gene expression analyses reveal distinct molecular signatures between differentially reprogrammed cardiomyocytes, Cell Rep. 20 (2017) 3014–3024, https://doi.org/10.1016/j.celrep.2017.09.005.

[11] A. Acun, T.D. Nguyen, P. Zorlutuna, In vitro aged, hiPSC-origin engineered heart tissue models with age-dependent functional deterioration to study myocardial infarction, Acta Biomater. 94 (2019) 372–391, https://doi.org/10.1016/j.actbio.2019.05.064.

[12] M. Wanjare, L. Hou, K.H. Nakayama, J.J. Kim, N.P. Mezak, O.J. Abilez, E. Tzatzalos, J.C. Wu, N.F. Huang, Anisotropic microfibrous scaffolds enhance the organization and function of cardiomyocytes derived from induced pluripotent stem cells, Biomater. Sci. 5 (2017) 1567–1578, https://doi.org/10.1039/c7bm00323d.

[13] L. Ren, X. Zhou, R. Nasiri, J. Fang, X. Jiang, C. Wang, M. Qu, H. Ling, Y. Chen, Y. Xue, M.C. Hartel, P. Tebon, S. Zhang, H.-J. Kim, X. Yuan, A. Shamloo, M. R. Dokmeci, S. Li, A. Khademhosseini, S. Ahadian, W. Sun, Combined effects of electric stimulation and microgrooves in cardiac tissue-on-a-chip for drug screening, Small Methods 4 (2020) 2000438, https://doi.org/10.1002/smtd.202000438.

[14] S. Liu, Z. Wang, X. Chen, M. Han, J. Xu, T. Li, L. Yu, M. Qin, M. Long, M. Li, H. Zhang, Y. Li, L. Wang, W. Huang, Y. Wu, Multiscale anisotropic scaffold integrating 3D printing and electrospinning techniques as a heart-on-a-chip platform for evaluating drug-induced cardiotoxicity, Adv. Healthcare Mater. 12 (2023) e2300719, https://doi.org/10.1002/adhm.202300719.

[15] A.-B. Siddique, A. Shanmugasundaram, J.Y. Kim, A. Roshanzadeh, E.-S. Kim, B.-K. Lee, D.-W. Lee, The effect of topographical and mechanical stimulation on the structural and functional anisotropy of cardiomyocytes grown on a circular PDMS diaphragm, Biosens. Bioelectron. 204 (2022) 114017, https://doi.org/10.1016/j.bios.2022.114017.

[16] A. Körner, M. Mosqueira, M. Hecker, N.D. Ullrich, Substrate stiffness influences structural and functional remodeling in induced pluripotent stem cell-derived cardiomyocytes, Front. Physiol. 12 (2021) 710619, https://doi.org/10.3389/fphys.2021.710619.

[17] G. Ye, Z. Wen, F. Wen, X. Song, L. Wang, C. Li, Y. He, S. Prakash, X. Qiu, Mussel-inspired conductive Ti2C-cryogel promotes functional maturation of cardiomyocytes and enhances repair of myocardial infarction, Theranostics 10 (2020) 2047–2066, https://doi.org/10.7150/thno.38876.

[18] B. Lu, M. Ye, J. Xia, Z. Zhang, Z. Xiong, T. Zhang, Electrical stimulation promotes the vascularization and functionalization of an engineered biomimetic human cardiac tissue, Adv. Healthcare Mater. 12 (2023) 2300607, https://doi.org/10.1002/adhm.202300607.

[19] P. Wu, X. Sai, Z. Li, X. Ye, L. Jin, G. Liu, G. Li, P. Yang, M. Zhao, S. Zhu, N. Liu, P. Zhu, Maturation of induced pluripotent stem cell-derived cardiomyocytes and its therapeutic effect on myocardial infarction in mouse, Bioact. Mater. 20 (2022) 286–305, https://doi.org/10.1016/j.bioactmat.2022.05.024.

[20] C. Tu, B.S. Chao, J.C. Wu, Strategies for improving the maturity of human induced pluripotent stem cell-derived cardiomyocytes, Circ. Res. 123 (2018) 512–514, https://doi.org/10.1161/CIRCRESAHA.118.313472.

[21] J.W. Miklas, S.S. Nunes, A. Sofla, L.A. Reis, A. Pahnke, Y. Xiao, C. Laschinger, M. Radisic, Bioreactor for modulation of cardiac microtissue phenotype by combined static stretch and electrical stimulation, Biofabrication 6 (2014) 024113, https://doi.org/10.1088/1758-5082/6/2/024113.

[22] W. Dou, A. Daoud, X. Chen, T. Wang, M. Malhi, Z. Gong, F. Mirshafiei, M. Zhu, G. Shan, X. Huang, J.T. Maynes, Y. Sun, Ultrathin and flexible bioelectronic arrays for functional measurement of iPSC-cardiomyocytes under cardiotropic drug administration and controlled microenvironments, Nano Lett. 23 (2023) 2321–2331, https://doi.org/10.1021/acs.nanolett.3c00017.

[23] D.A. Pijnappels, M.J. Schalij, A.A. Ramkisoensing, J. van Tuyn, A.A.F. de Vries, A. van der Laarse, D.L. Ypey, D.E. Atsma, Forced alignment of mesenchymal stem cells undergoing cardiomyogenic differentiation affects functional integration with cardiomyocyte cultures, Circ. Res. 103 (2008) 167–176, https://doi.org/10.1161/CIRCRESAHA.108.176131.

[24] C. Wang, S. Qiao, Y. Zhao, H. Tian, W. Yan, X. Hou, R. Wang, B. Zhang, C. Yang, F. Zhu, Y. Jiao, J. Jin, Y. Chen, W. Tian, The KLF7/PFKL/ACADL axis modulates cardiac metabolic remodelling during cardiac hypertrophy in male mice, Nat. Commun. 14 (2023) 959, https://doi.org/10.1038/s41467-023-36712-9.

[25] K. Han, J. He, L. Fu, M. Mao, Y. Kang, D. Li, Engineering highly-aligned three-dimensional (3D) cardiac constructs for enhanced myocardial infarction repair, Biofabrication 15 (2022), https://doi.org/10.1088/1758-5090/ac94f9.

[26] S. Choi, K.Y. Lee, S.L. Kim, L.A. MacQueen, H. Chang, J.F. Zimmerman, Q. Jin, M. M. Peters, H.A.M. Ardoña, X. Liu, A.-C. Heiler, R. Gabardi, C. Richardson, W.T. Pu, A.R. Bausch, K.K. Parker, Fibre-infused gel scaffolds guide cardiomyocyte alignment in 3D-printed ventricles, Nat. Mater. 22 (2023) 1039–1046, https://doi.org/10.1038/s41563-023-01611-3.

[27] D.S. Veliz, K.-L. Lin, C. Sahlgren, Organ-on-a-chip technologies for biomedical research and drug development: a focus on the vasculature, Smart Med. 2 (2023) e20220030, https://doi.org/10.1002/SMMD.20220030.

[28] L. Sun, H. Chen, D. Xu, R. Liu, Y. Zhao, Developing organs-on-chips for biomedical applications, Smart Med. 3 (2024) e20240009, https://doi.org/10.1002/SMMD.20240009.

[29] Y. Shang, D. Xu, L. Sun, Y. Zhao, L. Sun, A biomimetic optical cardiac fibrosis-on-a-chip for high-throughput anti-fibrotic drug screening, Research 7 (2024) 471, https://doi.org/10.34133/research.0471.

[30] D. Motlagh, S.E. Senyo, T.A. Desai, B. Russell, Microtextured substrata alter gene expression, protein localization and the shape of cardiac myocytes, Biomaterials 24 (2003) 2463–2476, https://doi.org/10.1016/s0142-9612(02)00644-0.

[31] A.O.-T. Wong, N. Wong, L. Geng, M.Z. Chow, E.K. Lee, H. Wu, M. Khine, C.-W. Kong, K.D. Costa, W. Keung, Y.-F. Cheung, R.A. Li, Combinatorial treatment of human cardiac engineered tissues with biomimetic cues induces functional maturation as revealed by optical mapping of action potentials and calcium transients, Front. Physiol. 11 (2020), https://doi.org/10.3389/fphys.2020.00165.

[32] S. Lv, J. Nie, Q. Gao, C. Xie, L. Zhou, J. Qiu, J. Fu, X. Zhao, Y. He, Micro/nanofabrication of brittle hydrogels using 3D printed soft ultrafine fiber molds for damage-free demolding, Biofabrication 12 (2020) 025015, https://doi.org/10.1088/1758-5090/ab57d8.

[33] D. Loessner, C. Meinert, E. Kaemmerer, L.C. Martine, K. Yue, P.A. Levett, T.J. Klein, F.P.W. Melchels, A. Khademhosseini, D.W. Hutmacher, Functionalization, preparation and use of cell-laden gelatin methacryloyl–based hydrogels as modular tissue culture platforms, Nat. Protoc. 11 (2016) 727–746, https://doi.org/10.1038/nprot.2016.037.

[34] K. Yue, G. Trujillo-de Santiago, M.M. Alvarez, A. Tamayol, N. Annabi, A. Khademhosseini, Synthesis, properties, and biomedical applications of gelatin methacryloyl (GelMA) hydrogels, Biomaterials 73 (2015) 254–271, https://doi.org/10.1016/j.biomaterials.2015.08.045.

[35] S. Lee, E.S. Sani, A.R. Spencer, Y. Guan, A.S. Weiss, N. Annabi, Human-recombinant-elastin-based bioinks for 3D bioprinting of vascularized soft tissues, Adv. Mater. 32 (2020) 2003915, https://doi.org/10.1002/adma.202003915.

[36] D. Huang, T. Liu, J. Liao, S. Maharjan, X. Xie, M. Pérez, I. Anaya, S. Wang, A. Tirado Mayer, Z. Kang, W. Kong, V.L. Mainardi, C.E. Garciamendez-Mijares, G. García Martínez, M. Moretti, W. Zhang, Z. Gu, A.M. Ghaemmaghami, Y. S. Zhang, Reversed-engineered human alveolar lung-on-a-chip model, Proc. Natl. Acad. Sci. U. S. A. 118 (2021) e2016146118, https://doi.org/10.1073/pnas.2016146118.

[37] P.W. Burridge, E. Matsa, P. Shukla, Z.C. Lin, J.M. Churko, A.D. Ebert, F. Lan, S. Diecke, B. Huber, N.M. Mordwinkin, J.R. Plews, O.J. Abilez, B. Cui, J.D. Gold, J. C. Wu, Chemically defined generation of human cardiomyocytes, Nat. Methods 11 (2014) 855–860, https://doi.org/10.1038/nmeth.2999.

[38] L. Sala, B.J. van Meer, L.G.J. Tertoolen, J. Bakkers, M. Bellin, R.P. Davis, C. Denning, M.A.E. Dieben, T. Eschenhagen, E. Giacomelli, C. Grandela, A. Hansen, E.R. Holman, M.R.M. Jongbloed, S.M. Kamel, C.D. Koopman, Q. Lachaud, I. Mannhardt, M.P.H. Mol, D. Mosqueira, V.V. Orlova, R. Passier, M.C. Ribeiro, U. Saleem, G.L. Smith, F.L. Burton, C.L. Mummery, MUSCLEMOTION: a versatile open software tool to quantify cardiomyocyte and cardiac muscle contraction in vitro and in vivo, Circ. Res. 122 (2018) e5–e16, https://doi.org/10.1161/CIRCRESAHA.117.312067.

[39] C. Darkes-Burkey, R.F. Shepherd, Volumetric 3D printing of endoskeletal soft robots, Adv. Mater. (2024) e2402217, https://doi.org/10.1002/adma.202402217.

[40] W. Liu, X. Zhang, X. Jiang, B. Dai, L. Zhang, Y. Zhu, Decellularized extracellular matrix materials for treatment of ischemic cardiomyopathy, Bioact. Mater. 33 (2024) 460–482, https://doi.org/10.1016/j.bioactmat.2023.10.015.

[41] H. Savoji, L. Davenport Huyer, M.H. Mohammadi, B.F. Lun Lai, N. Rafatian, D. Bannerman, M. Shoaib, E.R. Bobicki, A. Ramachandran, M. Radisic, 3D printing of vascular tubes using bioelastomer prepolymers by freeform reversible embedding, ACS Biomater. Sci. Eng. 6 (2020) 1333–1343, https://doi.org/10.1021/acsbiomaterials.9b00676.

[42] C.C. Kartha, Cardiomyocytes in Health and Disease, Springer International Publishing, Cham, 2021, https://doi.org/10.1007/978-3-030-85536-9.

[43] E. Karbassi, A. Fenix, S. Marchiano, N. Muraoka, K. Nakamura, X. Yang, C. E. Murry, Cardiomyocyte maturation: advances in knowledge and implications for regenerative medicine, Nat. Rev. Cardiol. 17 (2020) 341–359, https://doi.org/10.1038/s41569-019-0331-x.

[44] H. Qasim, M. Rajaei, Y. Xu, A. Reyes-Alcaraz, H.Y. Abdelnasser, M.D. Stewart, S. K. Lahiri, X.H.T. Wehrens, B.K. McConnell, AKAP12 upregulation associates with PDE8A to accelerate cardiac dysfunction, Circ. Res. 134 (2024) 1006–1022, https://doi.org/10.1161/CIRCRESAHA.123.323655.

[45] S. Min, S. Kim, W.-S. Sim, Y.S. Choi, H. Joo, J.-H. Park, S.-J. Lee, H. Kim, M.J. Lee, I. Jeong, B. Cui, S.-H. Jo, J.-J. Kim, S.B. Hong, Y.-J. Choi, K. Ban, Y.-G. Kim, J.-U. Park, H.-A. Lee, H.-J. Park, S.-W. Cho, Versatile human cardiac tissues engineered with perfusable heart extracellular microenvironment for biomedical applications, Nat. Commun. 15 (2024) 2564, https://doi.org/10.1038/s41467-024-46928-y.

[46] M. Böhm, A. Abdin, J. Slawik, F. Mahfoud, J. Borer, I. Ford, K. Swedberg, L. Tavazzi, C. Batailler, M. Komajda, Time to benefit of heart rate reduction with ivabradine in patients with heart failure and reduced ejection fraction, Eur. J. Heart Fail. 25 (2023) 1429–1435, https://doi.org/10.1002/ejhf.2870.

[47] J. Wang, S. Liu, X. Meng, X. Zhao, T. Wang, Z. Lei, H.I. Lehmann, G. Li, P. Alcaide, Y. Bei, J. Xiao, Exercise inhibits doxorubicin-induced cardiotoxicity via regulating B cells, Circ. Res. 134 (2024) 550–568, https://doi.org/10.1161/CIRCRESAHA.123.323346.

[48] L. Wang, Y. Qiao, J. Yu, Q. Wang, X. Wu, Q. Cao, Z. Zhang, Z. Feng, H. He, Endurance exercise preconditioning alleviates ferroptosis induced by doxorubicin-induced cardiotoxicity through mitochondrial superoxide-dependent AMPKα2 activation, Redox Biol. 70 (2024) 103079, https://doi.org/10.1016/j.redox.2024.103079.

[49] G. Zuo, X. Ren, X. Qian, P. Ye, J. Luo, X. Gao, J. Zhang, S. Chen, Inhibition of JNK and p38 MAPK-mediated inflammation and apoptosis by ivabradine improves cardiac function in streptozotocin-induced diabetic cardiomyopathy, J. Cell. Physiol. 234 (2019) 1925–1936, https://doi.org/10.1002/jcp.27070.